

Magnetic properties and field-induced phenomena in the $J_{\text{eff}} = 1/2$ distorted kagome antiferromagnet

A. Yadav¹, A. Elghandour², T. Arh³, D. T. Adroja^{4,5}, M. D. Le⁵, G. B. G. Stenning⁵, M. Aouane⁵, S. Luther⁶, F. Hotz⁷, T. J. Hicken⁷, H. Luetkens⁷, A. Zorko^{3,8}, R. Klingeler², and P. Khuntia^{1,9,*}

¹Department of Physics, Indian Institute of Technology Madras, Chennai 600036, India

²Kirchhoff Institute of Physics, Heidelberg University, INF 227, D-69120 Heidelberg, Germany

³Jožef Stefan Institute, Jamova c. 39, SI-1000 Ljubljana, Slovenia

⁴ISIS Facility, Rutherford Appleton Laboratory, Chilton, Didcot, Oxon, OX11 0QX, United Kingdom

⁵Highly Correlated Matter Research Group, Physics Department, University of Johannesburg, Auckland Park 2006, South Africa

⁶Dresden High Magnetic Field Laboratory, Helmholtz-Zentrum Dresden-Rossendorf, 01328 Dresden, Germany

⁷Laboratory for Muon Spin Spectroscopy, Paul Scherrer Institute, CH-5232 Villigen, Switzerland

⁸Faculty of Mathematics and Physics, University of Ljubljana, Jadranska u. 19, SI-1000 Ljubljana, Slovenia

⁹Quantum Centre of Excellence for Diamond and Emergent Materials, Indian Institute of Technology Madras, Chennai 600036, India.

(Dated: July 12, 2024)

The intertwining between competing degrees of freedom, anisotropy, and frustration-induced quantum fluctuations offers an ideal ground to realize exotic quantum phenomena in the rare-earth-based kagome lattice. Herein, we report synthesis, structure, thermodynamic, muon spin relaxation (μSR), nuclear magnetic resonance (NMR), and inelastic neutron scattering (INS) studies on a frustrated quantum magnet Nd_3BWO_9 wherein Nd^{3+} ions constitute a distorted kagome lattice. The INS experiments on Nd_3BWO_9 allow us to establish a detailed crystal electric field spectrum. The magnetic susceptibility reveals the presence of two energy scales in agreement with the INS results. The higher energy state is dominated by crystal field excitations, where the lowest Kramers ground-state doublet is well separated from the excited state suggesting that the compound realizes a low-energy $J_{\text{eff}} = 1/2$ state at low temperatures. The second energy scale is witnessed via thermodynamic results that reveal an anomaly at 300 mK typical of a phase transition, which is attributed to the presence of complex magnetic ordering phenomena. The broad maximum in the specific heat well above 0.3 K indicates the presence of short-range spin correlations that is corroborated by muon spin relaxation rate results. The isothermal magnetization reveals a field-induced $1/3$ magnetization plateau at low temperatures. μSR relaxation rate experiments, on the other hand, neither show the signature of a phase transition nor spin-freezing down to 34 mK. The zero field μSR relaxation is governed by an Orbach process and reveals the presence of a fluctuating state owing to depopulation of crystal field levels reflected as a constant value of relaxation rate in the temperature range $0.4 \leq T \leq 10$ K. NMR results indicate the presence of fluctuating Nd^{3+} moments down to 1.8 K consistent with μSR experiments. Our comprehensive results reveal that a field-induced quantum critical phenomenon is at play in this frustrated kagome magnet and enable us to construct a phase diagram exemplifying the proximity effect of competing magnetic states. This sets the stage to investigate the broad RE_3BWO_9 family of rare-earth kagome magnets promising to host exotic quantum states driven by spin-orbit coupling and frustration.

*pkhuntia@iitm.ac.in

I. INTRODUCTION

Geometrically frustrated magnets, wherein the incompatibility of exchange interactions between the spins in minimizing the ground state energy lead to macroscopic ground state degeneracy, non-trivial low-energy excitation spectra, and quantum phase transitions, represent a mainstream field of modern condensed matter [1]. Quantum mechanical effects such as spin-orbit coupling, entanglement, and quantum fluctuations, as well as the non-trivial topology of the electron wave function of frustrated quantum materials, offer an incredible ground to realize intriguing quantum and topological states such as quantum spin liquid (QSL) with exotic quasi-particle excitations [2, 3]. QSL is a highly entangled state of quantum matter wherein frustration-induced strong quantum fluctuations evade magnetic long-range ordering down to absolute zero temperature despite strong exchange interaction between spins. QSL is promising to host fractional excitations that are coupled to emergent gauge fields and QSL has the potential to address some of the recurring themes in quantum condensed matter and is highly relevant for topological quantum computing [1–3]. In this context, the frustrated kagome antiferromagnet with corner-sharing triangles of magnetic moments renders an emblematic two-dimensional (2D) model that can maximize frustration-induced quantum fluctuations and is a promising contender to host exotic quantum phenomena [5–10]. In particular, quantum spin liquids [11–13], magnetization plateaus [14], incommensurate magnetic order [15], and chiral spin-ordered states [16], massive Dirac fermions in ferromagnetic kagome metal, anomalous Hall effect [17–19], Berry phase [20], and unconventional superconductivity [21–22] in kagome magnets represent an appealing track in contemporary quantum matter to establish theoretical models that could resemble the properties of experimental candidates [23, 24]. A weak perturbation in the nearest-neighbor Heisenberg model, such as next-nearest neighbor interactions, anisotropy, including the Dzyaloshinskii-Moriya interaction, in kagome magnets, can have a striking effect on the underlying spin Hamiltonian and ground state properties. [1,4, 25–34. Quantum criticality is also at play in diverse QSL models and frustrated magnets, which suggests that non-thermal external tuning parameters, i.e., pressure and magnetic field, can drive a quantum phase transition at $T \rightarrow 0$, exemplifying the competition between the nearly degenerate phases that have very similar characteristic energy scales [4–6,35].

The rare-earth-based frustrated kagome quantum magnet with distinct magnetic ions is a promising candidate to stabilize a structurally perfect lattice comprising a highly tunable nature of weak exchange interactions mediated by strongly localized magnetic moments. In these kagome materials, the synergistic interplay between strong spin-orbit coupling and crystal electric field (CEF) often generates an exchange anisotropy, which often leads to effective spin-1/2 degrees of freedom that are prone to strong quantum fluctuations at low temperatures, thus offering an excellent route to stabilize many-body quantum states [2–7, 36–43]. However, defects and anti-site disorder pose a strong constraint for the unambiguous identification of the ground-state properties of these kagome antiferromagnets. Despite being intensively investigated, the exact origin of QSL states in most of the $3d$ and $4f$ materials remains elusive but is now believed to be closely related to structural disorder and defects. The current challenge is to design, discover, and investigate structurally perfect kagome antiferromagnet representatives that provide a viable platform to host fascinating quantum states. In this vein, the recently discovered rare-earth family RE_3BWO_9 (RE= rare-earth elements) where R^{3+} ions form a distorted-kagome lattice in the xy -plane and are stacked along the z -axis provides an alternate

route to realize spin orbit driven correlated quantum states with non-trivial low-energy excitation spectra [44]. For instance, $R_3\text{BWO}_9$ ($R = \text{Gd, Dy, and Ho}$) shows a large magnetocaloric effect under the application of an external magnetic field, which is highly relevant for magnetic refrigeration at low temperatures. Pr_3BWO_9 exhibits a dynamic ground state down to 0.03 K with Ising-like spin correlations, while Sm_3BWO_9 hosts an incommensurate magnetic order. Nd_3BWO_9 is also a promising candidate to host frustration and field-induced quantum states, including a 1/3 magnetization plateau, and unconventional quantum critical phenomena at low temperatures [45-50]. However, details concerning spin-freezing, local magnetic field distribution at low temperatures, and a comprehensive crystal electric field scheme are not yet clear for the kagome magnet Nd_3BWO_9 . Moreover, detailed insights into the ground state properties by local probe techniques such as NMR and μSR are missing.

Herein, we present synthesis, magnetization, specific heat, muon spin relaxation, NMR, and inelastic neutron scattering results on the polycrystalline samples of the spin-orbit-driven frustrated $4f$ magnet Nd_3BWO_9 . Our thermodynamic results reveal the realization of a $J_{\text{eff}} = 1/2$ state in the lowest Kramers doublet, which is well separated from the excited states, as confirmed by our inelastic neutron scattering experiments. Thermodynamic results reveal the presence of a weak antiferromagnetic interaction between Nd^{3+} moments ($J_{\text{eff}} = 1/2$) at low temperatures. In addition, thermodynamic results point towards a magnetically ordered state below ~ 0.3 K and short-range spin correlations above 0.8 K. The muon spin relaxation results do not detect spin-freezing or magnetic ordering down to 34 mK. The μSR relaxation rate is driven by an Orbach mechanism and dynamic electronic moments. NMR results are consistent with thermodynamic and μSR results. A fractionalized magnetization plateau has been observed in a magnetization isotherm recorded at low temperatures, suggesting that a phenomenological order-by-order mechanism is active in this frustrated magnet. Our comprehensive results enable us to establish a rich magnetic phase diagram that suggests that a complex field-induced magnetic phenomenon is at play in this spin-orbit-driven frustrated kagome magnet, which is located in the proximity of a quantum critical point.

II. EXPERIMENTAL DETAILS

Polycrystalline samples of Nd_3BWO_9 (henceforth NBWO) were synthesized following a standard solid-state reaction route. Stoichiometric amounts of Nd_2O_3 (Alfa Aesar, 99.999%), H_3BO_3 (Alfa Aesar, 98%), and WO_3 (Alfa Aesar, 99.998%) were taken as starting materials [44, 51]. Since H_3BO_3 is highly volatile, we have taken 5% of the excess to maintain proper stoichiometry in the sample. Nd_2O_3 was preheated at 900°C overnight to remove moisture and carbonates prior to use. The reagents were thoroughly mixed to achieve better homogeneity. The pellets were annealed in an alumina crucible in the temperature range of $700\text{--}900^\circ\text{C}$ with several intermediate grindings. The non-magnetic analog used for inelastic scattering and heat capacity studies was prepared following the same method. For INS experiments, boron-11-enriched samples were synthesized. The x-ray diffraction (XRD) data were taken on the polycrystalline sample of Nd_3BWO_9 using a benchtop PANalytical diffractometer with $\text{CuK}\alpha$ radiation ($\lambda = 1.541 \text{ \AA}$) at room temperature.

The DC magnetization measurements on NBWO were performed in the temperature range of $1.8 \leq T \leq 350$ K using a Magnetic Properties Measurement System (MPMS3, Quantum Design). For measurements down to 400 mK, the MPMS3 was equipped with the iQuantum He3 setup. The DC magnetization data were obtained following zero-field and field-cooled protocols. The AC magnetization measurements were conducted in the temperature range from 1.8 to 60 K with 5–7 Oe AC excitation fields, up to 5 Tesla DC magnetic fields, and frequencies ranging from 10 Hz to 0.8 kHz using the AC option of the MPMS3. To measure the specific heat of the sample, a thermal relaxation method was employed using the specific heat option of the Physical Property Measurement System (PPMS, Quantum Design). For NBWO, the measurements were carried out in the temperature range of 0.06 to 2 K using a dilution refrigerator (DR) in zero field on PPMS from Quantum Design. Pulsed-field magnetization was measured up to 60 T at the Helmholtz Zentrum Dresden-Rossendorf by an induction method using a coaxial pick-up coil system where a pulse raising time of 7 ms was used [52]. The pulsed-field magnetization data were calibrated using magnetization data recorded in the static magnetic field on MPMS, Quantum Design. The field dependence of magnetization obtained by the two methods is in good agreement, confirming the accuracy of our experiments.

Inelastic neutron scattering measurements were carried out at the ISIS Neutron and Muon Source on the MARI time-of-flight spectrometer on Nd_3BWO_9 powder samples (samples prepared with an enriched 11-B isotope). The experiments were carried out using a close-cycle refrigerator (CCR) and a Fermi chopper with the Gd-slit package. We collected data at 5 K with a neutron incident energy of $E_i = 80$ meV and a Fermi-chopper speed of 250 Hz. We also measured the phonon reference compound La_3BWO_9 in identical conditions.

Muon spin relaxation (μSR) experiments were performed on GPS and FLAME spectrometers at the Swiss muon source at PSI in Villigen, Switzerland, in zero field and longitudinal field configurations. The measurements on the GPS instrument were performed down to 1.6 K on a pressed pellet 10 mm in diameter and 1.6 mm thick. The pellet was secured between two 25- μm Cu foils and fastened to a copper fork sample holder. Additionally, the FLAME spectrometer equipped with a Variox plus Kevinox dilution fridge insert was used for zero field (ZF) and longitudinal field (LF) μSR measurements in a wide temperature range between 0.034 and 300 K. The μSR data were analyzed to extract relevant parameters to shed insights into the ground state properties of the present material using the musrfit program [53].

^{11}B NMR ($I = 3/2$) measurements were carried out using a home-built spectrometer and Oxford magnet with a fixed field of approximately 9.4 T (Larmor frequency of 128.321 MHz). A flow cryostat was used to cover the temperature range between 4 and 300 K. A 133 mg powder sample was used for these measurements. The NMR spectra were recorded by sweeping the frequency and combining individual spectra obtained via the standard Hahn-echo pulse sequence. The ^{11}B spin-lattice relaxation was measured by employing the inversion recovery pulse sequence.

III. RESULTS

A. Structural details

The XRD data taken at room temperature confirms the phase purity of the samples studied in this work. To determine the structural parameters, Rietveld refinement of the XRD data was performed using GSAS software. The Rietveld refinement of the XRD data reveals no detectable atomic disorder in this material [Fig. 1(a-b)]. It reveals that NBWO crystallizes in a hexagonal structure with space group $P6_3$. In this material, Nd^{3+} ions constitute a distorted kagome spin-lattice in the xy -plane that is stacked along the z -axis. The refinement parameters are consistent with earlier reports [44] and are summarized in Table I. It is observed that the Nd^{3+} ions form NdO_8 dodecahedrons with oxygen ions which are distorted due to the slightly different Nd-O bond lengths, i.e., 2.7 Å, 3 Å, and 2.6 Å, resulting in a distorted kagome lattice in the xy -plane as shown in Fig. 1(a), which suggests a complex exchange network in this frustrated magnet [44, 48, 51]. The presence of a structural phase transition has been ruled out by the specific heat result presented in the next section.

Table I: The atomic parameters obtained from the Rietveld refinement of x-ray diffraction data of Nd_3BWO_9 , recorded at room temperature. (Space group: $P6_3$, $a = b = 8.6891\text{Å}$, $c = 5.4936\text{Å}$, $\alpha = \beta = 90^\circ$, $\gamma = 120^\circ$ and $\chi^2=1.36$, $R_{\text{wp}}=4.21\%$, $R_p=3.26\%$, and $R_{\text{exp}}=3.61\%$).

Atom	Wyckoff position	x	y	z	Occupancy
Nd	$6c$	0.358	0.083	0.220	1
B	$2a$	0.000	0.000	0.693	1
W	$2b$	0.333	0.666	0.249	1
O ₁	$6c$	0.141	0.044	0.867	1
O ₂	$6c$	0.202	0.459	0.023	1
O ₃	$6c$	0.109	0.481	0.497	1

B. Magnetization

The response of magnetization in the presence of an external applied magnetic field reveals interesting insights concerning exchange interactions, anisotropy, and spin correlations in NBWO. The temperature dependence of dc magnetic susceptibility taken in an external magnetic field of 0.1 T is shown in Fig. 1(c). The dc magnetic susceptibility shows neither signature of long-range magnetic order nor spin freezing down to 1.8 K. The fit of the inverse of dc magnetic susceptibility data above 150 K with the Curie-Weiss law yields an effective moment $\mu_{\text{eff}} = 3.7(1)\mu_B$ as expected for free ion value $\mu_{\text{eff}}^{\text{free}} = 3.62\mu_B$ of Nd^{3+} ion ($4f^3$, $^4I_{9/2}$) and the Curie-Weiss temperature $\Theta_{\text{CW}} = -46(2)$ K. The negative value of Θ_{CW} corresponds to the energy scale of crystal-electric-field excitations [4]. The inverse magnetic susceptibility shows a change of slope below 100 K indicating repopulation of crystal electric field (CEF) levels. The Curie-Weiss fit of inverse magnetic susceptibility data below 40 K yields an effective moment $\mu_{\text{eff}} = 2.96(1)\mu_B$, which is small compared to the free ion moment value indicating a low energy state with $J_{\text{eff}}=1/2$ at low temperatures that might support strong quantum fluctuations. The reduced effective

moment in the low temperature fit indicates that only some crystal field levels contribute to the susceptibility below 40 K, and thus there must be an energy gap between these low-lying levels and higher energy levels such that above 150 K we recover the full expected effective moment.

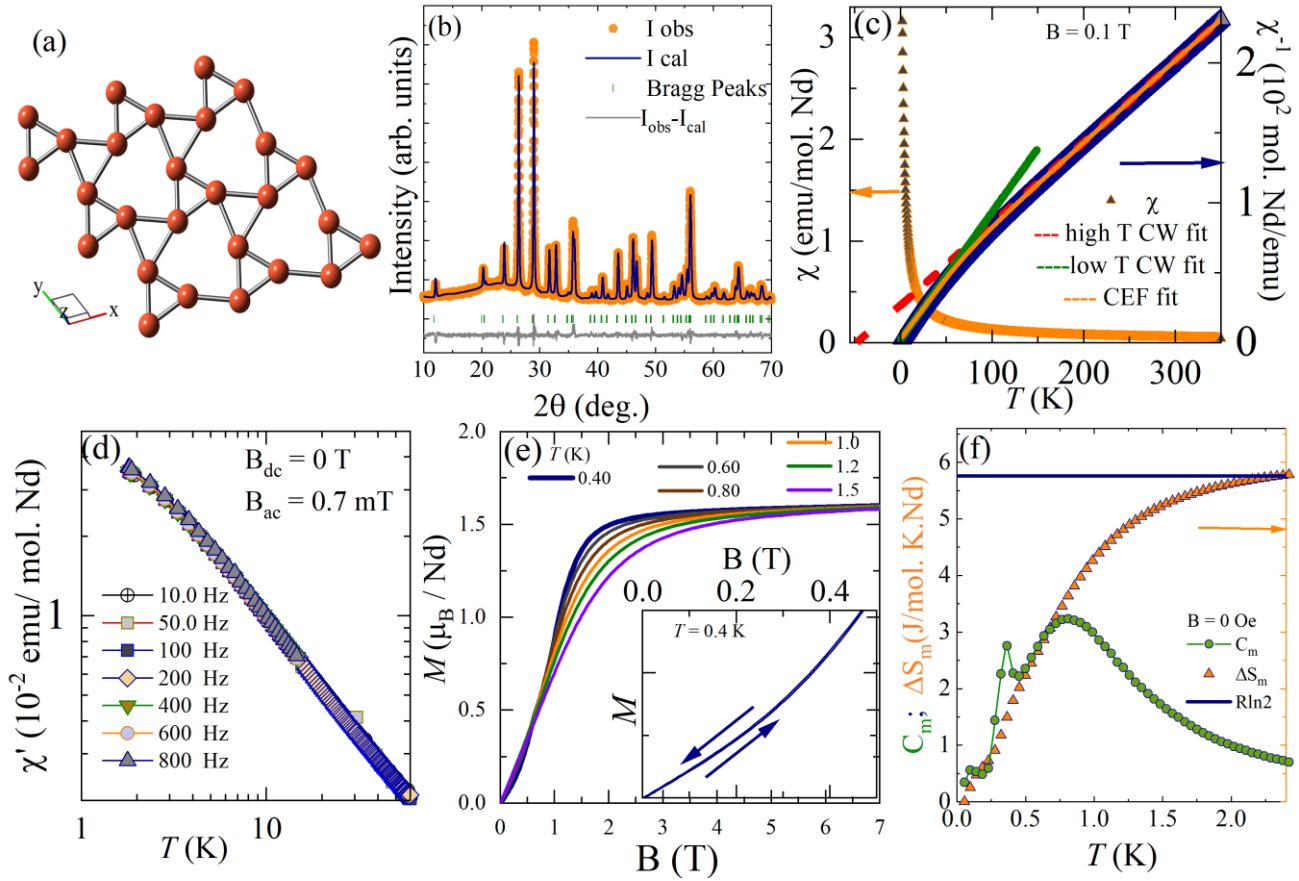


Fig.1 (a) Kagome lattice constituted by Nd^{3+} ions in the xy -plane of Nd_3BWO_9 . (b) Rietveld refinement of xrd data taken at room temperature. (c) The temperature dependence of magnetic susceptibility in 0.1 T (left) taken in ZFC mode and inverse magnetic susceptibility with Curie-Weiss and two level CEF fits as discussed in the text (right). (d) AC susceptibility recorded at different frequencies in zero dc field and 0.7 mT ac field. (e) Magnetization isotherms at several temperatures. The inset shows the low-field magnetization isotherm at 0.4 K for better clarity. (f) The temperature dependence of specific heat taken in zero field at low temperature. The magnetic entropy in zero field that saturates to a value $R\ln 2$ reflecting a low energy $J_{\text{eff}}=1/2$ Kramer doublet ground state at low temperatures.

The corresponding Curie-Weiss temperature, $\theta_{\text{CW}} = -2.8$ (1) K represents the energy scale of exchange interaction between Nd^{3+} ($J_{\text{eff}}=1/2$) moments at low temperatures. The crystal electric field affects the magnetic susceptibility at high temperatures in 4f magnets. In NBWO, it splits the tenfold degenerate $J=9/2$ multiplet into five Kramers doublets of Nd^{3+} ion. The lowest Kramers doublet with $J_{\text{eff}}=1/2$ at low temperatures is well separated from the excited states as revealed by our inelastic neutron scattering experiments as discussed in section B. The $J_{\text{eff}}=1/2$ lowest Kramers state mainly governs the low-temperature physics of this frustrated magnet. The

mean field approximation, $J_{ex} = -\frac{3k_B\theta_{CW}}{zS(S+1)}$ (where $z = 4$ and $S=J_{\text{eff}}=1/2$ in the present case) yields an exchange interaction $J_{ex}/k_B = 2.8$ (2) K. The presence of weak exchange interaction is typical of $4f$ magnets owing to strong localization of rare-earth ions that is comparable with the dipolar interaction [36]. Our low temperature specific heat data reveal a phase transition around 0.3 K (see Fig. 1f), which is possibly due to an extra term in the magnetic Hamiltonian leading to a complex magnetic ordering phenomena. The frustration parameter, $f = \frac{|\theta_{CW}|}{T_N}$, quantifying the degree of frustration, is thus close to 10, suggesting a highly frustrated spin-lattice that enhances quantum fluctuations, leading to suppressed magnetic ordering at ~ 0.3 K as discussed in the following section.

As depicted in Fig. 1(c), we can reconcile the two energy scales in the inverse magnetic susceptibility of Nd^{3+} ion using a simple two-level model (a simple approximation assuming that there are two levels) [54] as described below, and also from a full fitting of the crystal field levels to inelastic neutron data in section B.

$$\frac{1}{\chi(T)} = \frac{8(T - \theta_{CW}) (1 + e^{-\Delta/k_B T})}{\mu_{1\text{eff}}^2 + \mu_{2\text{eff}}^2 e^{-\Delta/k_B T}}$$

where $\frac{\Delta}{k_B} = 215$ (10) K is the gap between the ground state Kramers doublet and the first excited CEF level, $\mu_{1\text{eff}} = 3$ (1) μ_B is the effective moment of the ground state, and $\mu_{2\text{eff}} = 4.2$ (2) μ_B is the effective moment of the first excited state. The Curie-Weiss temperature $\theta_{CW} = -3$ (2) K is related to the exchange interaction between Nd^{3+} moments in the Kramers ground state. The large value of CEF gap ($\frac{\Delta}{k_B}$), reflected as a change of slope of inverse susceptibility data below 100 K, suggests that the Kramers doublet ground state is well separated from the excited states, which is in reasonable agreement with that obtained from the inelastic neutron scattering experiment. As shown in Fig. 1(d), the ac susceptibility at different magnetic fields rules out a spin-glass state down to 1.8 K. The absence of hysteresis in the magnetization isotherm at 400 mK (see Fig. 1(e)) adds further credence to the claim. The magnetic-specific heat obtained after subtracting the lattice and nuclear-specific heat shows a broad maximum around 0.8 K, and on further lowering the temperature, an antiferromagnetic phase transition is observed at 0.3 K, as shown in Fig. 1(f). As presented in Fig. 1(f), the magnetic entropy extracted from the specific heat data saturates to a value that corresponds to $R\ln 2$ at low temperatures, which suggests the realization of a low-energy $J_{\text{eff}}=1/2$ state in the ground state Kramers doublet in agreement with magnetic susceptibility.

C. Crystal Electric Field Spectrum

The magnetism of the frustrated kagome magnet Nd_3BWO_9 is innately connected to the crystal electric field scheme of Nd^{3+} ion. To investigate the crystal field excitations, and anisotropy and to probe the energy and wave vector dependence of the dynamic structure factor in Nd_3BWO_9 , we have performed INS experiments on MARI spectrometer. Fig.2 (a) shows the Q-integrated (0 to 4 \AA^{-1}) INS spectra from low wave vector Q in Nd_3BWO_9 . It shows magnetic scattering

estimated after subtracting the phonon using the nonmagnetic La_3BWO_9 data [55]. We have observed four well defined CEF excitations from the ground state CEF doublet of Nd^{3+} (ground multiplet $J = 9/2$, which splits into 5 CEF doublets in the C_1 point symmetry of Nd^{3+} ions in the paramagnetic state), in Nd_3BWO_9 (Fig. 2b), which indicate the localized nature of $4f$ -electron in this kagome magnet. The solid line shows the fit based on the CEF analysis and the values of CEF parameters obtained are given in the Appendix-A, Tables II and III.

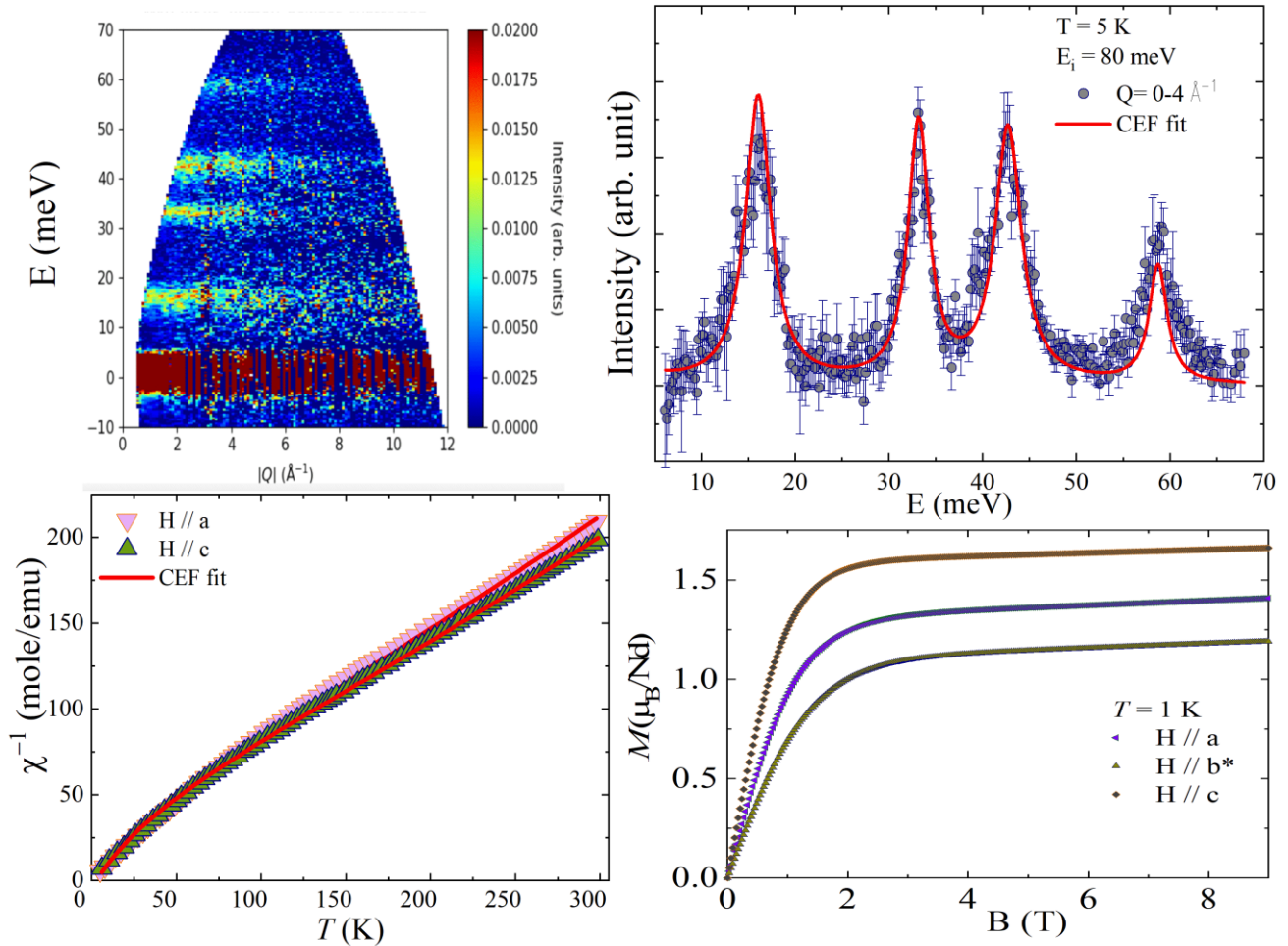


Fig. 2 (a) Inelastic neutron scattering intensity of Nd_3BWO_9 obtained after subtraction of phonon contribution using the non-magnetic reference La_3BWO_9 at 5 K for the incident energy $E_i=80$ meV (b) Q integrated (0 to 4 \AA^{-1}) E vs. Intensity-cut from the INS data taken with $E_i=80$ meV at 5 K with fit to the CEF model shown by the solid line. (c) The temperature dependence inverse magnetic susceptibility data of the single crystals adapted from ref. [49] compared with calculated inverse magnetic susceptibility in different crystallographic directions using the CEF parameters as provided in the appendix. (d) Calculated magnetization isotherm at 1 K in three crystallographic directions with relevant CEF parameters.

The CEF parameters were estimated by fitting the INS spectra and magnetic susceptibility taken on the single crystals together (see Appendix for more details). The fit to the inverse susceptibility data is shown in Fig. 2c. We also simulated the magnetization isotherms in

different directions using the CEF parameters and the results are plotted in Fig.2d, which also agree well with the experimental M vs. H results on the single crystals of NBWO [49]. The value of the gap suggests that the lowest Kramers doublet is well separated with a gap of 186(8) K from the excited states confirming the thermodynamics and μ SR results. Thus, the ground state physics of this kagome antiferromagnet could be mapped by the low energy state $J_{\text{eff}}=1/2$ corroborating thermodynamic results. The $J_{\text{eff}}=1/2$ state arises due to strong spin-orbit coupling and crystal electric field prone to strong quantum fluctuations at low temperatures and likely to dominate ground state of this frustrated magnet.

D. AC susceptibility and specific heat

AC susceptibility is a sensitive probe to track ground state properties and spin dynamics in frustrated magnets. AC susceptibility measurements were performed in zero DC field and in AC excitation magnetic fields in a wide frequency range (10Hz to 800 kHz) to delineate spin dynamics and shed insights into field-induced effects in this kagome antiferromagnet. As shown in Fig. 1d, the real part of AC susceptibility (χ'_{ac}) recorded in an AC field of 7 Oe increases monotonically upon decreasing temperature without any signature of magnetic ordering down to 1.8 K, which is consistent with the DC magnetic susceptibility.

The frequency-independent behavior of AC susceptibility rules out the presence of spin-glass behavior at least down to 1.8 K. This suggests that the characteristic fluctuation rate of Nd^{3+} moments is beyond the time scale of AC susceptibility experiment. Fig. 3 (a-b) depicts the AC susceptibility taken in several DC fields with an AC excitation field of 7 Oe at a frequency 10 Hz. The real part of AC susceptibility (χ'_{ac}) in DC magnetic fields shows a field-induced behavior at around 7 K and a noticeable change of slope with strong DC fields (Fig. 3b). Notably, the imaginary part of the AC susceptibility (χ''_{ac}) exhibits a broad maximum ~ 4.3 K in DC magnetic fields of 0.5 T, and the position of the maximum shifts towards higher temperature upon increasing magnetic field. Contrastingly, the amplitude of χ''_{ac} starts decreasing with a DC magnetic field ≥ 2 T [56]. The magnetic origin of the broad maximum in specific heat at ~ 0.8 K in zero field is confirmed by Fisher's specific heat $\left(\frac{d(\chi T)}{dT}\right)$ calculated from the DC susceptibility recorded down to 0.4 K (see Fig.3(c)). It is worth noting that this maximum is independent of the measurement protocol (ZFC-FC) and is insensitive to magnetic field up to 0.1 T. However, the 0.8 K maximum flattens with magnetic field above 0.4 T and shifts towards lower temperature and completely disappears with a field ≥ 0.9 T. Interestingly, the magnetic specific heat shows an anomaly at ~ 0.4 K in a field of 0.9 T, which indicates that a field-induced phenomenon is at play in this kagome antiferromagnet. This is indeed consistent with the presence of anomaly in isothermal magnetization recorded at low temperatures as discussed in the next paragraph. In order to single out potential magnetic ordering, we have performed magnetization and specific heat measurements also in the sub-Kelvin temperature range given weak interaction energy scale in this localized $4f$ magnet.

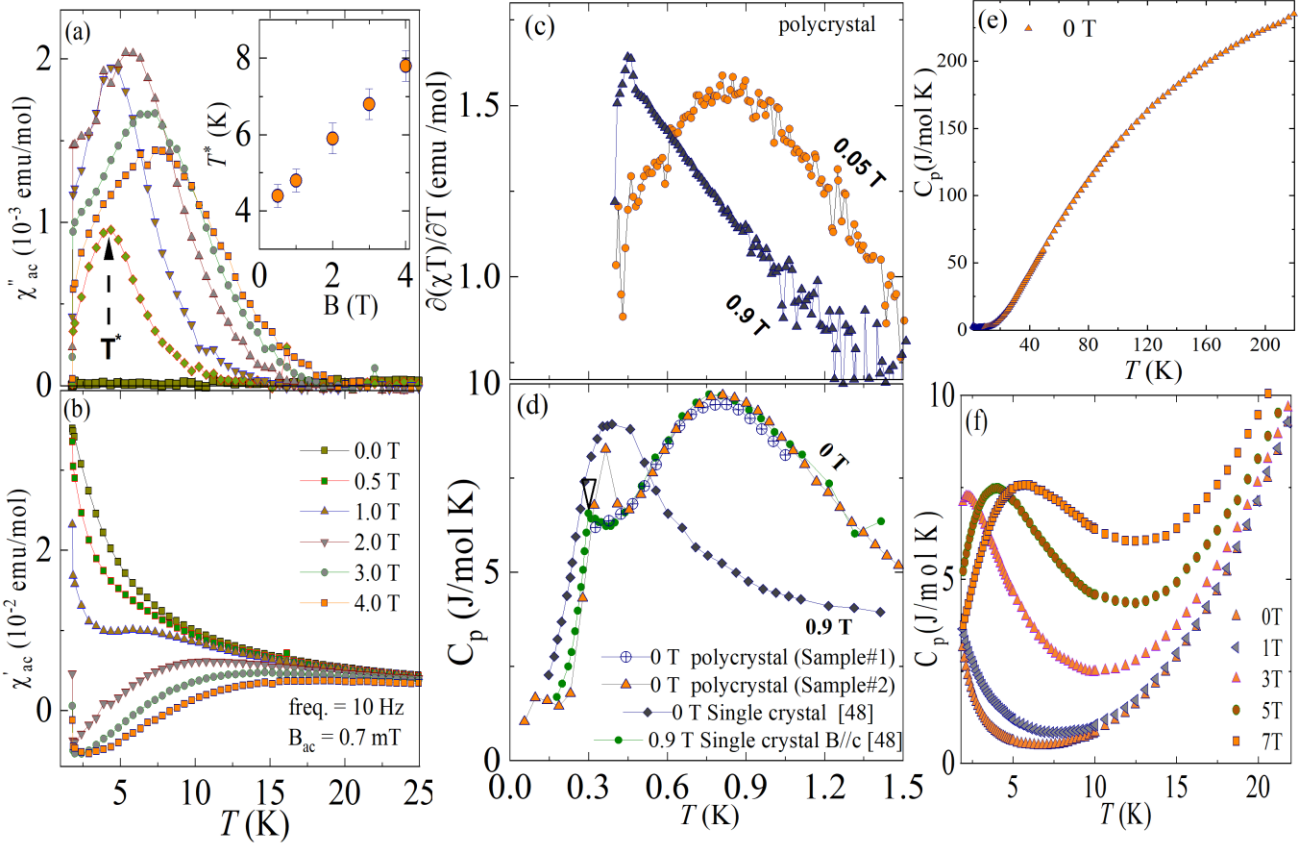


Fig.3. The temperature dependence of the imaginary part of the ac susceptibility and the inset shows the variation of broad maxima (T^*) in the imaginary part of AC susceptibility with DC magnetic field (b) The temperature dependence of the real part of the ac susceptibility in different DC fields taken at 10 Hz and ac field 0.7 mT. (c) The temperature dependence of Fisher specific heat determined from dc susceptibility measured in 0.05 T and 0.9 T (d) The temperature dependence of specific heat in the polycrystalline samples of Nd_3BWO_9 that is compared with the single crystal data adapted from ref. [48]. (e) The temperature dependence of specific heat in zero field in the temperature range $1.8 \leq T \leq 220$ K rules out the presence of any structural phase transition. (f) The temperature dependence of specific heat taken in different applied fields at low temperature.

Fig. 3d depicts the temperature dependence of specific heat in zero field that is compared with that taken on the single crystals adapted from ref. [48]. The specific heat shows a sharp anomaly at ~ 0.3 K typical of long-range magnetic ordering. The anomaly at 0.3 K is sensitive to applied magnetic field and it smears out with the magnetic field. The specific heat shows a broad peak around 0.4 K in an external magnetic field of 0.9 T. The appearance of a broad maximum in specific heat around 0.8 K in the absence of a magnetic field is a characteristic feature of short-range spin correlations. The specific heat in the temperature range from 1.8 K to 220 K (See Fig. 3(e)) don't show any anomalies that suggest the absence of a structural phase transition in the temperature range of investigation in this material. Fig. 3(f) shows the temperature dependence of specific heat in different external applied magnetic fields. As shown in Fig. 3(f), the broad maximum shifts in a Schottky-like manner toward higher temperature upon increasing the magnetic field indicating a field-polarized state. The field-induced gap that scaled

with magnetic field is ascribed to the Zeeman splitting of the lowest Kramers doublet $J_{\text{eff}}=1/2$ at low temperatures (not shown here).

To shed more insight into the effect of magnetic field on the low-temperature magnetic phase, we have performed magnetization measurements down to 400 mK and in magnetic fields up to 60 T. Fig. 4(a) shows the isothermal magnetization recorded at 400 mK in Nd_3BWO_9 . The absence of hysteresis rules out any secondary phases or spin glass behavior in this frustrated kagome material. The magnetization increases with field up to 0.4 T followed by a quasi-plateau wherein the orientation of the magnetic moment changes much less with the external applied magnetic field. This is consistent with the $1/3 M_{\text{sat}}$ magnetization plateau and eventually saturates to a value of $M_{\text{sat}} = 1.5 \mu_B/\text{Nd}$, as shown in Fig. 4(a), in line with what was found in the single crystals [48,49]. The observed features in the magnetization isotherm at 400 mK imply a complex magnetic structure wherein phenomenologically, two spins in a triangle of the host kagome lattice might align with the external magnetic field while one spin in each triangle points opposite to the applied magnetic field, known as the uud phase. This exotic magnetic phase is associated with an “order-by-disorder” mechanism due to the fact that quantum fluctuations lift ground state degeneracy and adopt specific spin configurations at low temperatures in frustrated magnets. [1, 55, 56, 57]. Upon further increase of the magnetic field, the magnetization isotherm at 400 mK saturates completely to a constant value $\sim 1.5 \mu_B/\text{Nd}^{3+}$ in an external magnetic field of 4 T. As shown in Fig.4(b), the derivative of isothermal magnetization dM/dB at 400 mK reveals many interesting features, namely, a shoulder-like anomaly, two peaks corresponding to critical fields B_{c1} , B_{c2} related to the beginning and end of magnetization plateau and a minimum at B_{min} at the center of the magnetization plateau [58]. The shoulder-like anomaly shifts to the lower magnetic field side and vanishes upon increasing the temperature above 0.5 K. The anomalies at B_{c1} and B_{min} slightly shift to the higher field side and also eventually disappear at $T > 0.5$ K. The peak at B_{c2} shifts to the lower magnetic field side upon increasing the temperature and disappears within a broad hump at $T \geq 0.8$ K. This intriguing low-temperature behavior of the magnetization suggests that a complex field-induced quantum phenomenon is at play in this spin-orbit driven kagome antiferromagnet.

Fig. 4(c-d) represent a comparative account of the magnetization isotherms taken at different temperatures using a static field and pulsed magnetic field up to 60 T. The high-field magnetization isotherm at a low temperature of ~ 540 mK saturates in the low field regime and increases with field in the high field limit (Fig. 4(c)). The high-field magnetization isotherm at 11.5 K shows non-linear behavior over a wide field range, as shown in Fig. 4(c). The fit of the magnetization isotherm at 11.5 K to a Brillouin function taking into account the paramagnetic Nd^{3+} ions with total angular momentum, $J=9/2$, doesn't reproduce the experimental data, which suggests the persistence of spin-correlations in this temperature range. However, adding a linear term to the Brillouin function $M_{\text{sat}}B(x) + \chi_0 B$, where $x = \frac{g\mu_B JB}{k_B T}$, fits the magnetization isotherm at 11.5 K (Fig. 4(d)). The linear term in the high-field magnetization isotherm indicates the presence of short-range spin correlations that are consistent with the enhancement of temperature dependence of magnetic susceptibility and NMR shift at low temperatures, as discussed in subsequent sections.

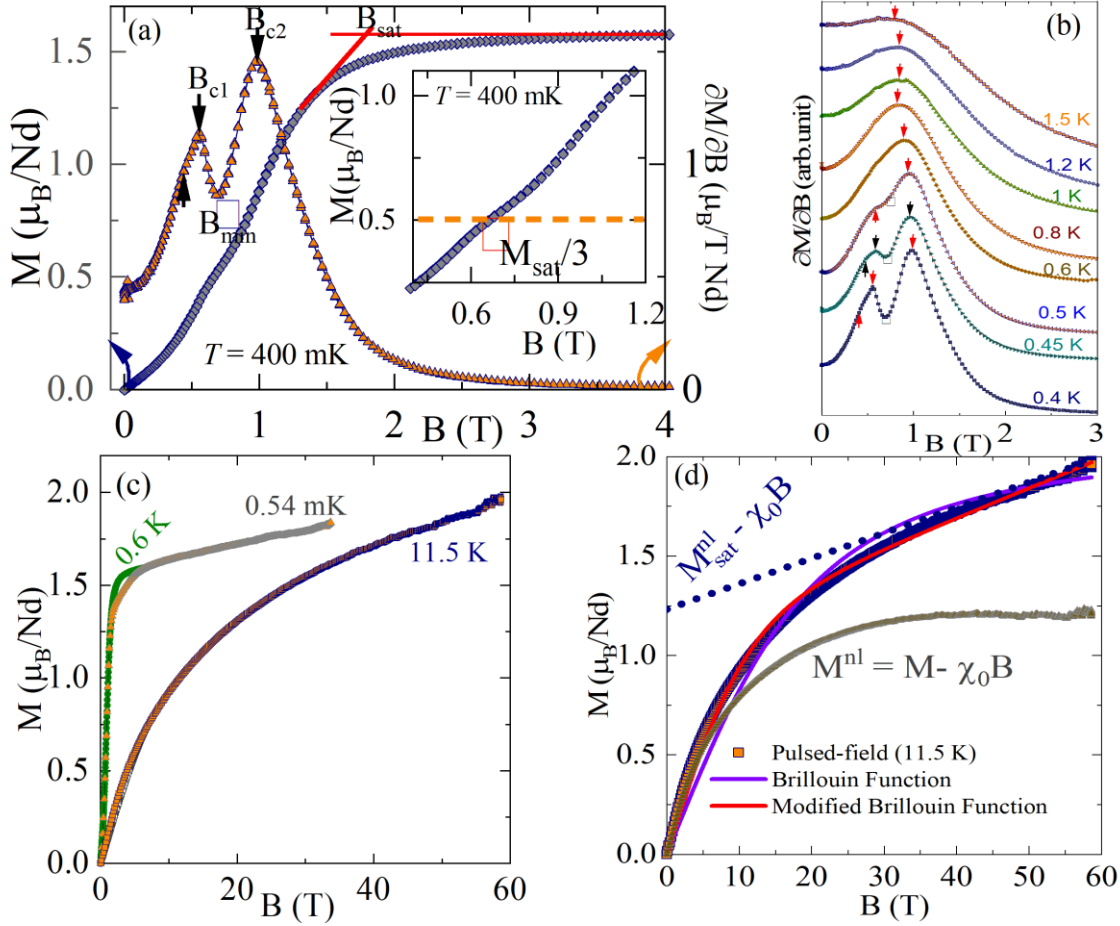


Fig. 4. (a) Magnetization isotherm recorded at 400 mK (left). The derivative of magnetization ($\partial M/\partial B$) with respect to magnetic field (right) is also shown to track the critical fields associated with some field induced phases at low temperature. The inset shows the magnetization plateau at 400 mK. (b) The derivative of magnetization isotherms ($\partial M/\partial B$) taken at different temperature to identify the evolution of field induced phases in an external applied magnetic field. (c) Magnetization isotherm measured up to 60 T at different temperatures using pulsed magnetic field. The pulsed field data are compared with that taken in a static magnetic field. (d) Magnetization isotherm at 11.5 K taken using pulsed high magnetic field up to 60 T. The solid lines depict the simulation following Brillouin and modified Brillouin functions as discussed in the text.

The distinct anomalies in the temperature dependence of specific heat and field dependence of magnetization enable us to construct a comprehensive magnetic phase diagram, reflecting the presence of several interesting field-induced phases in this antiferromagnet (Fig. 5). This is compared with the earlier reported phase diagram on the single crystals of Nd_3BWO_9 [48, 56]. We observed that the phase labeled as A forms a confined dome that spans over a field range 0-0.6 T which also exists for the magnetic fields applied along a^* and c crystallographic directions. This A phase is hardly magnetizable up to a field of 0.5 T as evident from the magnetization isotherm taken at 120 mK [48] suggesting a gapped excitation spectrum in this field. At low temperature $T = 120$ mK, Nd_3BWO_9 hosts field-induced phases namely, B and C in a field >0.6 T

applied along a^* and c axes, respectively [48]. Interestingly, both B and C phases exhibit similar $1/3$ magnetization plateaus, the magnetic order within the phases is different, the B phase spanning over $0.55-1.2$ T is characterized by wave vector $Q(0,1/2,1/2)$ while the wave vector $Q(1/3,1/3,1/3)$ characterizes the C phase in the magnetic field range $0.55 \leq \mu_0 H \leq 1$ T [48]. The polycrystalline sample of Nd_3BWO_9 hosts a field-induced dome-like phase D, as depicted in Fig. 5, which is reminiscent of that found in the single crystals [48,56].

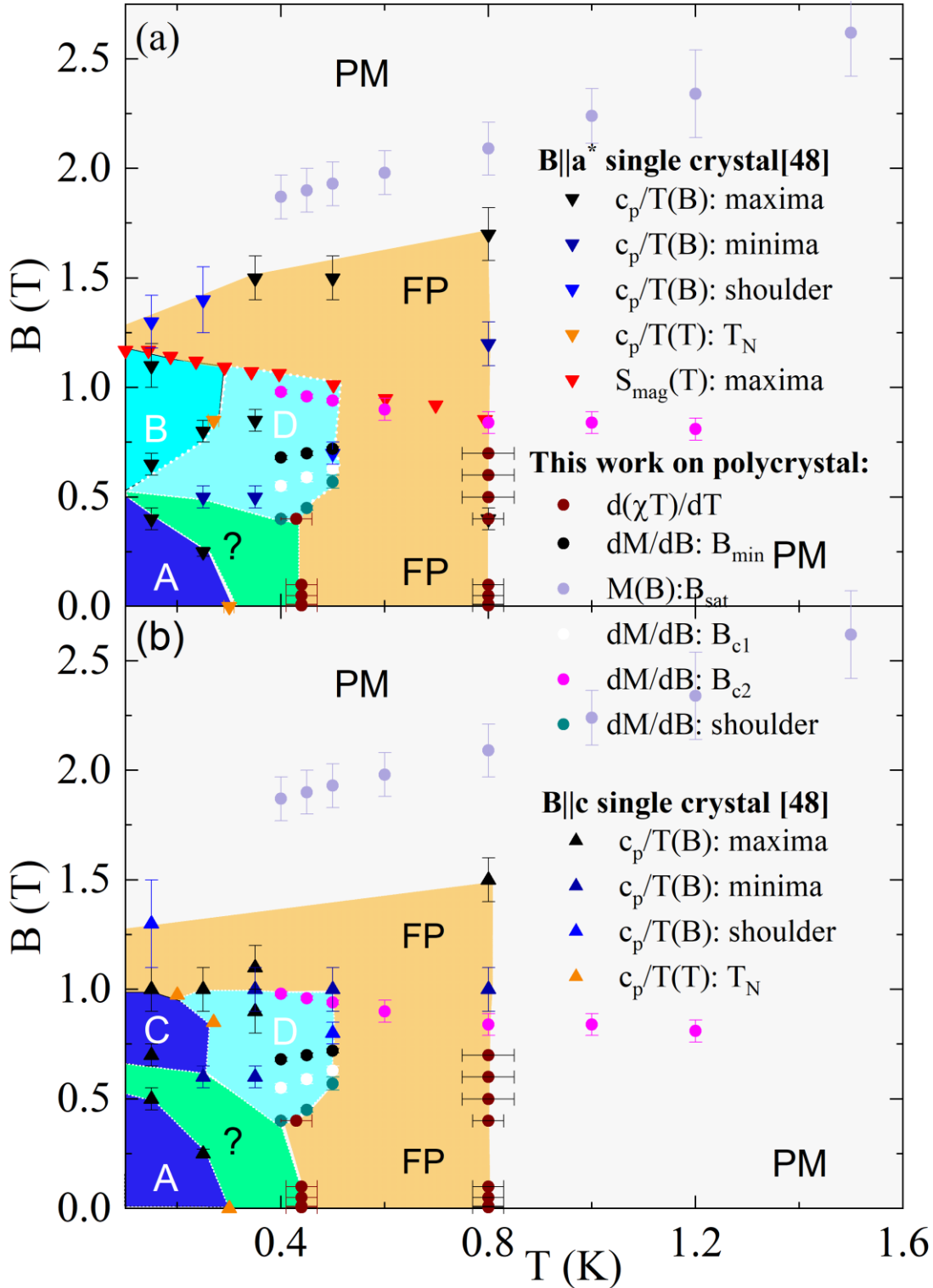


Fig. 5. (a,b) The field induced magnetic phases (FP- Field polarized; PM-Paramagnetic) of NBWO derived from magnetization and specific heat results as discussed in the text. The two figures compare our polycrystal data with measurements on single crystal for magnetic field applied (a) $B||a$ and (b) $B||c$ directions, respectively. Our data confirm several previously known phase boundaries but also imply additional magnetic phases in this kagome antiferromagnet (marked green and within phase D) [48].

The presence of magnetization plateau and dome shaped phases both in single crystal and polycrystalline samples suggest that D is a magnetically ordered phase in this spin-orbit driven kagome antiferromagnet. Remarkably, the specific heat, C_p and Fisher specific heat derived from DC magnetic susceptibility, $\left(\frac{d(\chi T)}{dT}\right)$, data show a broad maximum around 0.8 K that is indicating a cross-over from a paramagnetic phase to a field-polarized state consistent with our magnetization experiments conducted at low temperatures. The Nd_3BWO_9 frustrated kagome material behaves like an unconventional paramagnet above 0.8 K.

E. Muon spin relaxation

In order to shed additional light to the magnetism of NBWO and track the local field distribution in real space as well as spin fluctuations, zero field (ZF) and longitudinal field (LF) μSR experiments were conducted over a wide temperature and field range.

E.1 ZF measurements

The μSR measurements were first performed in zero field (ZF) with the initial spin direction anti-parallel to the muon momentum. Fig. 6a depicts the ZF muon asymmetry at the lowest temperature of 34 mK. The absence of oscillations in the ZF muon asymmetry curve and the vanishing asymmetry at long times, i.e. the absence of the 1/3 tail, rule out static local magnetic fields at the muon stopping sites even at the lowest accessible temperature. The μSR asymmetry relaxes extremely quickly (note the logarithmic scale in Fig. 6a), however, it is composed of two contributions, one faster and one slower decaying. The attempts to fit the data with the stretched exponent relaxation function were unsuccessful, a model with two simple exponentially decaying components works much better. Thus, we use the model $A(t) = A_0(f \cdot e^{-\lambda_{\text{fast}}t} + (1 - f) \cdot e^{-\lambda_{\text{slow}}t})$, with the fraction of the fast component $f = 0.86(1)$ fixed from low-temperature data. The presence of two components is likely due to muons stopping at two magnetically inequivalent muon stopping sites in the host spin-lattice.

The temperature dependence of the muon spin relaxation rate of the dominant fast component in zero field is shown in Fig. 6(b). The muon relaxation rate increases by several orders of magnitude on cooling the sample from 300 to 20 K, where a relaxation plateau is established. The strong temperature dependence of the ZF relaxation rate is consistent with an Orbach relaxation mechanism, associated with crystal-field fluctuations, as observed in several frustrated magnets including $\text{NdTa}_7\text{O}_{19}$ [2, 57].

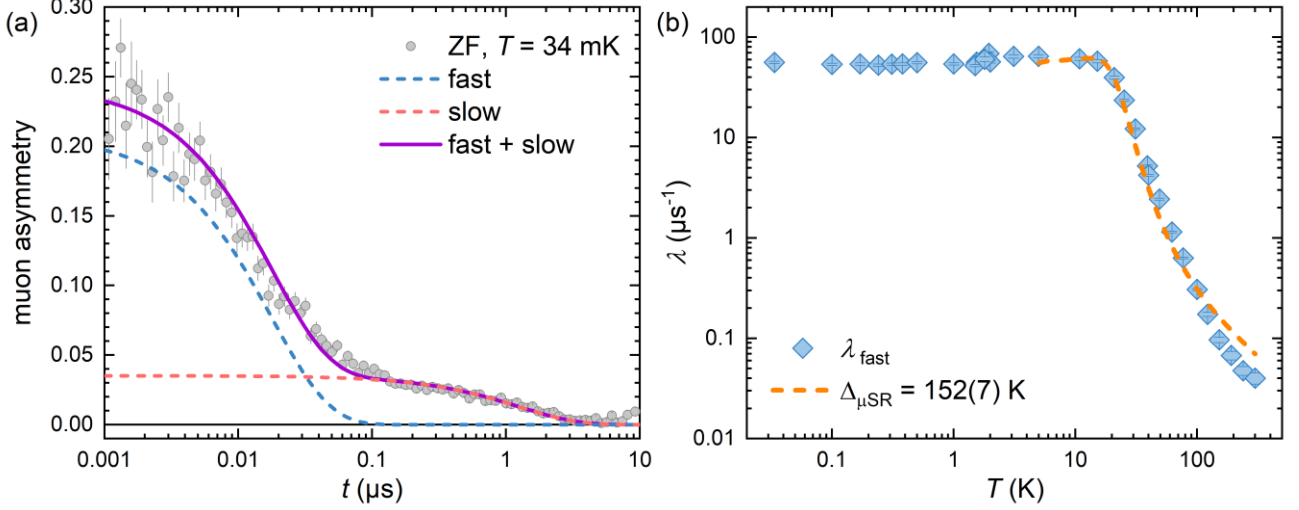


Fig. 6 (a) The ZF muon asymmetry dataset (points) at the base temperature with the two-component exponential fit (lines), as further explained in the text. (b) The temperature dependence of the ZF muon relaxation rate of the fast-relaxing dominant component. The dashed line depicts the model combining the temperature-independent and the Orbach relaxation mechanisms as explained in the text.

Assuming the fast fluctuation regime, the muon relaxation rate is inversely proportional to the frequency of spin fluctuations, $\lambda^{-1} \propto \nu_e$, which is described as a sum of two independent mechanisms,

$$\nu_e(T) = \nu_0 + \frac{\nu_1}{e^{\Delta_{\mu\text{SR}}/k_B T} - 1}. \quad (1)$$

Here, the temperature-dependent term is the Orbach term that dominates the relaxation rate above 20 K. The constant term that corresponds to the relaxation rate plateau is associated with the muon spin relaxation in the ground-state Kramers doublet. Such behavior of the relaxation rate suggests that at temperatures below 20 K effective spin-1/2 degrees of freedom emerge in the ground state, as the excited crystal-field states do not contribute anymore to the muon spin relaxation. The relaxation rate was modelled with Eq. (1) after combining the ZF and the LF measurements, which allowed for the determination of the coupling constant between λ^{-1} and ν_e , as shown in the next section.

E.2 LF measurements

To gain a more quantitative insight into the fluctuations of the Nd^{3+} magnetic moments, we performed LF measurements in a wide range of temperatures in three magnetic fields between 1.5 and 3.5 T.

The LF muon asymmetry curves were fitted with the same two-component exponential model as for ZF with the fraction of the two components fixed to $f = 0.86$, and the resulting fast-relaxing component is shown in Fig. 7a. In the fast fluctuation regime, the field and the temperature dependence of the relaxation rate is described by the Redfield model [58]

$$\frac{\lambda(T)}{\chi(T)T} = A_{\mu\text{SR}} \frac{\nu_e(T)}{\nu_e(T)^2 + \omega_L^2}. \quad (2)$$

Since the electron spin fluctuation frequency $\nu_e(T)$ monotonically increases with increasing temperature due to the Orbach process, a maximum appears in the muon spin relaxation rate at a temperature where ν_e crosses the Larmor frequency $\omega_L = \gamma_\mu B_0$ for each LF (Fig. 7a). From the maximum, we can extract the value of the coupling constant $A_{\mu SR}$ for the three applied fields. It is found to be field independent within the error bars, so we use its average value $A_{\mu SR} = 33.2 \cdot 10^3 \text{ mol}/(\text{K} \cdot \text{emu} \cdot \text{s}^2)$ to derive the temperature dependence of $\nu_e(T)$ for each field including the ZF measurement. This rate is found to be field independent in the investigated range between 0 and 3.5 T (Fig. 7b).

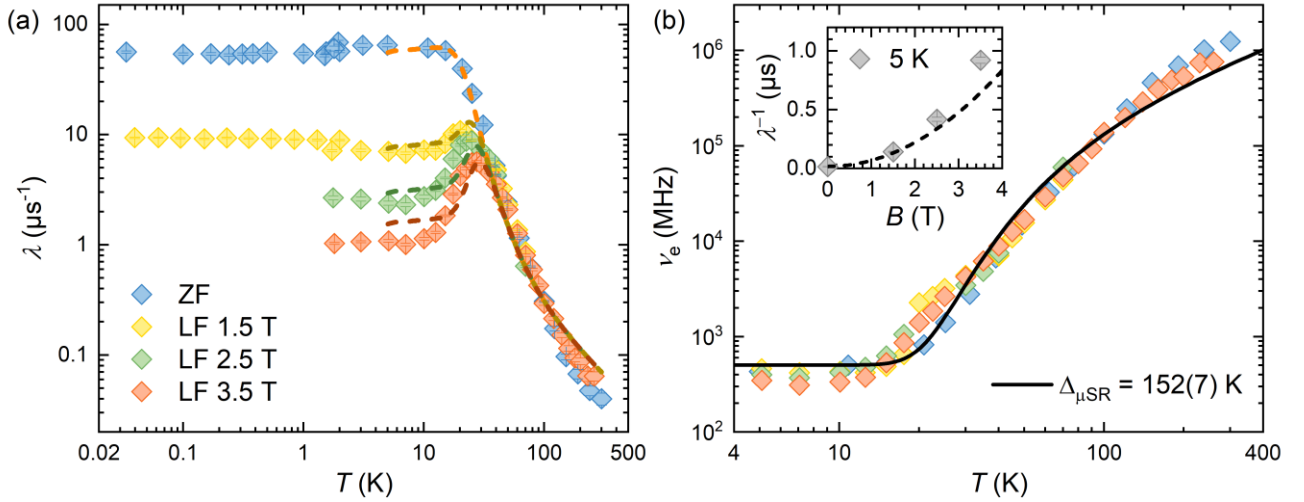


Fig. 7 (a) The temperature dependence of the muon spin relaxation rate of the dominant fast component and (b) the corresponding spin fluctuation rate ν_e (see text) at ZF and at several LFs. The inset shows the field dependence of the muon spin relaxation rate at 5 K. The solid line in panel (b) is a fit of ν_e in all magnetic fields to Eq. (1). The obtained model is then used to calculate the relaxation rates with Eq. (2), which are shown with the dashed lines in panel (a) and the inset.

The simultaneous fit of the four $\nu_e(T)$ datasets with a single-gap Orbach model plus a constant (Eq. (1), three free parameters) yields a low-temperature plateau of $\nu_0 = 504(43) \text{ MHz}$ and the gap of $\Delta_{\mu SR}/k_B = 152(7) \text{ K}$ that roughly matches the gap between the ground state and the first excited CEF level $\Delta/k_B = 186(8) \text{ K}$ that was measured via the INS, again revealing that the lowest Kramers doublet is well separated from the excited Kramers doublets. A similar scenario was observed in several rare-earth-based frustrated magnets [4, 57].

Finally, with the model for $\nu_e(T)$ and a coupling constant $A_{\mu SR}$ we can use Eq. (2) to reconstruct the temperature dependence of the muon spin relaxation data in all fields including the ZF (Fig. 7a), as well as its field dependence at 5 K (inset in Fig. 7b). Since we use a fairly simple model, the results at high temperatures are not described perfectly, likely due to higher CEF levels affecting the spin fluctuations, and there is some deviation at high fields as well. Nevertheless, the model is remarkably successful in describing the main features of the data in all fields. At low

temperatures, the spin fluctuating frequency $\nu_e = 504(43)$ MHz can be compared to the width of the fluctuating fields distribution at the muon stopping site of $B_{loc} = \gamma_\mu^{-1} \sqrt{A_{\mu SR} \chi(T) T / 2} = 0.14(4)$ T, which corresponds to $\gamma_\mu B_{loc} = 119(36)$ MHz. The assumption of the fast fluctuation regime ($\nu_e > \gamma_\mu B_{loc}$) was therefore justified even at low temperatures. It may be noted that μ SR does not detect an anomaly at 0.3 K, unlike thermodynamic experiments. One possible scenario for the absence of an anomaly at 0.3 K in μ SR results could be due to the fact that the homogeneous internal field at the two muon stopping sites cancelled out [59-61]. However, this seems unlikely, as both magnetically inequivalent sites would show this rather unusual effect simultaneously. A cancellation of internal fields has indeed been observed, e.g., for a highly symmetric muon site in the heavy-fermion compound UPd₂Al₃ [62]. However, even in this case, a weak anomaly is observed at the transition temperature due to imperfections in the magnetic structure. The absence of oscillations in the μ SR does not necessarily indicate the absence of long-range order. If slow magnetic fluctuations (in the MHz) are present together with static magnetism, the muon spin relaxation might be dominated by the magnetic fluctuations at low temperatures. Therefore, our μ SR study invokes the search for a persistent spin dynamic that coexists with the magnetic order indicated by the macroscopic techniques. Whether the emergence of exotic fractional excitations in frustrated magnets could lead to such a scenario is not clear at present, but it offers a new direction to carry out detailed investigations on the single crystals of NBWO in the future [63, 64].

F. Nuclear magnetic resonance

Nuclear magnetic resonance (NMR) is a powerful technique for providing microscopic insights into the intrinsic magnetic susceptibility and low energy spin dynamics. In NBWO, there is only one crystallographic site for boron, with the Wyckoff position $2a$. The ¹¹B NMR spectra shown in Fig. 7a consist of the central line and two satellite lines, as typical for $I = 3/2$ nuclei. The quadrupole frequency $\nu_Q \approx 1.3$ MHz is determined from the distance between the two satellite peaks. The spectra get increasingly broadened with lowering temperatures, the change in the spectrum is especially large between 45 K and 40 K. In the intermediate temperature range $10 \leq T \leq 40$ K, we are not able to measure the NMR spectra due to extremely short spin-spin relaxation times T_2 (Fig. 8b). Such NMR wipe-out was observed before in another Nd-based kagome system, the neodymium langasite [65,66]. However, the NMR signal reappears below 10 K due to the increase of the ¹¹B spin-spin relaxation time, in line with the slowing down of spin dynamics that observed in μ SR (Fig. 7b).

On cooling, the NMR spectra broaden and shift to lower frequencies. The ¹¹B NMR shift comprises of temperature dependent spin shift and temperature independent orbital/chemical shift $K_0 = 0.13(1)\%$; $K(T) = K_{spin} + K_0$. Here, K_{spin} scales with bulk magnetic susceptibility, i.e., $K_{spin}(T) = A_{hf} \chi(T)$, in the whole temperature range between 300 and 40 K where the position of the central line can be unambiguously determined (Fig. 8c). The fit yields the hyperfine coupling constant between nuclear and electronic spins, $A_{hf} = -0.178(4)$ T/ μ_B .

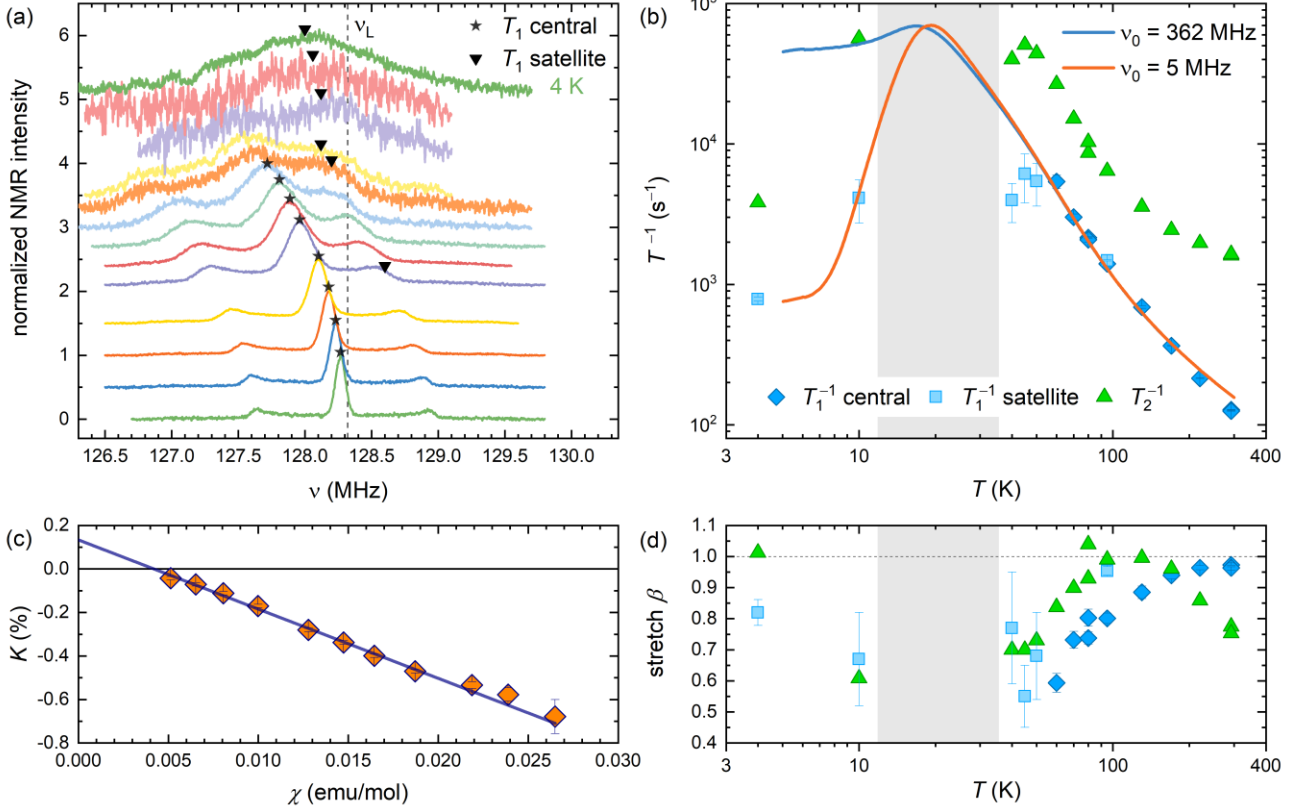


Fig.8 (a) The temperature evolution of ^{11}B NMR spectra recorded at 9.4 T. The dashed line corresponds to the Larmor frequency. Stars and triangles indicate the positions where T_1 measurements were conducted at a particular temperature. The scaling of the central line with bulk susceptibility is shown in (c) together with the linear fit (solid line). (b) The temperature dependence of the spin-lattice ($1/T_1$) and the spin-spin ($1/T_2$) relation rate and (d) the corresponding stretch exponents. The solid lines in (b) correspond to the fits of the BPP model to the $1/T_1$ dataset, as explained in the text.

In order to probe dynamic susceptibility associated with low-energy spin fluctuations, we also performed ^{11}B nuclear spin-lattice (T_1) relaxation time measurements [67]. The temperature dependence of the spin-lattice relaxation rate $1/T_1$ is shown in Fig. 8b. Above 50 K, it was measured at the maximum of the central line (stars in Fig. 8a), for which the inversion recovery curve of the longitudinal nuclear magnetization M was fitted by a multiexponential recovery curve valid for magnetic relaxation in the case of $I = 3/2$ nucleus,

$$M_z(t) = M_0 \left[1 - (1 + \alpha) \left\{ 0.1 \exp\left(-\left(\frac{t}{T_1}\right)^\beta\right) + 0.9 \exp\left(-\left(\frac{6t}{T_1}\right)^\beta\right) \right\} \right].$$

Here α is the inversion factor and β is the stretching exponent. The stretched exponential behaviour (i.e., $\beta < 1$ in Fig. 8d) suggests a distribution of relaxation times in the host spin-lattice. Below 50 K, $1/T_1$ was measured on the right satellite peak (triangles in Fig. 8a) due to better signal compared to the central line. Here, the magnetization was modelled with an expression appropriate for the satellite transition,

$$M_z(t) = M_0 \left[1 - (1 + \alpha) \left\{ 0.1 \exp\left(-\left(\frac{t}{T_1}\right)^\beta\right) + 0.5 \exp\left(-\left(\frac{3t}{T_1}\right)^\beta\right) + 0.4 \exp\left(-\left(\frac{6t}{T_1}\right)^\beta\right) \right\} \right].$$

In order to verify that the $1/T_1$ values from different parts of the spectra can be directly compared, we measured $1/T_1$ at both the central and the satellite transition at 95 K, where practically the same value was found (Fig. 7d).

The temperature dependence of $1/T_1$ matches the temperature dependence of the muon spin relaxation rate λ (Fig. 7a). In fact, we can use the same model as in the μ SR analysis,

$$\frac{1}{T_1 T \chi(T)} = A_{NMR} \frac{\nu_e(T)}{\nu_e(T)^2 + \omega_L^2},$$

which is in NMR known as the Bloembergen, Purcell and Pound (BPP) theory [67, 68]. In our NMR experiment, we cannot measure the spin-lattice relaxation at the maximum value (where $\nu_e(T) = \omega_L$), because of the wipe-out, therefore the coupling constant A_{NMR} cannot be determined from the experiment, as it was possible for $A_{\mu SR}$. Therefore, we use the same two-gap model with the parameters from the μ SR modelling, with the rescaled $A_{NMR} = 3500 A_{\mu SR}$ as the only free parameter. The resulting curve fits well with the experimental $1/T_1$ values in the temperature range between 300 and ~ 50 K (blue curve in Fig. 8b). However, at low temperatures this model fails to account for the experiment. A better agreement is obtained (red curve in Fig. 8b) if the plateau value of the fluctuation frequency is also a free parameter when the fit yields $\nu_0 = 5(1)$ MHz. The decrease of the low-temperature fluctuation rate from $\nu_0 = 457(43)$ MHz, as determined from μ SR, might be a result of a much stronger magnetic field applied in the NMR experiments (9.4 T) that should sufficiently polarize the spins at low temperatures. Alternatively, in the case of spin correlations, different local probes can filter spin fluctuations differently because of the site dependence of the form factor.

IV. DISCUSSION

Competing magnetic interaction and spin orbit-driven magnetic anisotropy conspire with quantum fluctuations in driving intriguing quantum phenomena in the distorted kagome antiferromagnet Nd_3BWO_9 . This is a distorted spin-lattice with corner-shared triangular motifs wherein inequivalent Nd-Nd bond distances and Nd-O-Nd bond angles most likely led to inequivalent exchange couplings in the host spin-lattice. The kagome planes are separated by a distance comparable to the intraplane bond distance. In this material with Nd^{3+} ($^4I_{9/2}$) ions, the crystal-field states comprise of five Kramers doublets, and the ground state with $J_{\text{eff}}=1/2$ is well separated from the first excited state by a gap of 186 (8) K, as evidenced by our inelastic neutron scattering experiments. The low-temperature physics of this Kagome antiferromagnet is governed by the exchange interaction between $J_{\text{eff}}=1/2$ moments. In the mean-field approximation, the antiferromagnetic exchange interaction between Nd^{3+} moments determined from the Curie-Weiss temperature obtained from the fit of magnetic susceptibility at low temperatures is $J_{\text{ex}}=2.8$ K (2). The presence of such a weak exchange interaction is typical of $4f$ magnetic moments in view of the localized nature of $4f$ orbitals [2–4]. Specific heat measurements show a sharp anomaly around 0.3 K, implying an antiferromagnetic phase transition that is associated with the presence of finite interplane interaction between $J_{\text{eff}}=1/2$ spins [49]. A broad maximum around 0.8 K in ZF specific heat and Fisher-specific heat derived from DC magnetic susceptibility well above the transition temperature evinces short-range spin-

correlations in this frustrated magnet. The low-temperature magnetization isotherm in the magnetically ordered state exhibits a plateau at $1/3$ of the saturation magnetization value in the presence of an external magnetic field of $\sim 0.5J_{\text{ex}}$. This unconventional behavior of low temperature magnetization isotherm in this frustrated kagome antiferromagnet is most likely related to a complex magnetic structure comprising up-up-down spin configurations of $J_{\text{eff}} = 1/2$ spins in the host spin-lattice, captured by a phenomenological order-by-disorder mechanism. [69-73]. This has been encountered in several frustrated $3d$ and $4f$ magnets with spontaneous breaking of translational symmetry [69-71]. In the $S=1/2$ Heisenberg model on a kagome lattice wherein spins interact via exchange coupling J_{ex} , the $1/3$ magnetization plateau is characterized by low-energy excitations in the magnetically ordered state with a Zeeman gap that scales with magnetic field $B = 2J_{\text{ex}}S$, which is indeed relevant in the present case [1, 69-73]. Notably, $S > 3/2$ kagome lattices with Heisenberg exchange and strong easy axis or single ion anisotropy show a magnetization plateau [68-70]. The broad maximum in specific heat is sensitive to magnetic field, and an anomaly develops with an applied magnetic field of 0.9 T, which suggests that the investigated frustrated magnet is located in close proximity of a quantum critical point. The zero field μSR relaxation rate is governed by the Orbach mechanism typical of rare-earth-based frustrated magnets with CEF splitting with a gap that is consistent with thermodynamic and INS results. ^{11}B NMR experiments unveil the presence of fluctuating electronic moments without the signature of magnetic ordering or freezing down to 1.8 K. The μSR asymmetry neither shows oscillations nor the $1/3$ tail down to 34 mK characteristic feature of long-range magnetic ordering and spin-freezing, respectively, which is at variance with that observed in specific heat. The absence of oscillations in muon asymmetry does not necessarily rule out magnetic order in this kagome magnet. One possible scenario could be that the co-existence of slow magnetic fluctuations along with static magnetism, and muon spin relaxation might be dominated by the slowly fluctuating magnetic moments at low temperatures. An interesting query is whether such an intriguing low-temperature magnetic state could harbor exotic fractional excitations in this frustrated magnet is not clear at present, but it provides a new direction to carry out detailed investigations on the single crystals of NBWO in the future [63, 64].

V. SUMMARY

The frustrated magnet Nd_3BWO_9 with Nd^{3+} moments embodying a distorted kagome spin-lattice is characterized by the interplay between spin-orbit coupling and spin correlations that leads to exotic magnetism and spin dynamics. The ground state Kramers doublet is well separated from the excited states, implying that the ground state can be described by $J_{\text{eff}} = 1/2$ spins, potentially leading to strong quantum fluctuations. The isothermal magnetization at sub-Kelvin temperature reveals a field-induced fractionalized magnetization plateau, suggesting an up-and-down ordered configuration of spins in each triangle of the frustrated kagome lattice with respect to the applied magnetic field. The specific heat, however, reveals the presence of a phase transition at 0.3 K that is attributed to the presence of interplane coupling between Nd^{3+} moments. The magnetic specific heat shows a broad maximum around 0.8 K, indicating the persistence of short-range spin correlations well above the magnetic phase transition temperature. The μSR relaxation at high temperatures is governed by an Orbach mechanism that is observed in several frustrated magnets based on rare earth ions. In addition, the μSR and NMR

experiments reveal the presence of fluctuating electronic moments. The absence of a $1/3$ tail in the muon asymmetry down to 34 mK rules out spin-freezing in this frustrated magnet, which is consistent with thermodynamic results. The absence of long-range magnetic ordering down to 34 mK, as revealed by our zero-field μ SR experiments, suggests the predominant role of slowly fluctuating magnetic moments along with static magnetism at low temperatures. A clear picture concerning this warrants a thorough investigation of the high-quality single crystals of Nd_3BWO_9 , which is beyond the scope of the present work. The external magnetic field drives several field-induced phases, implying the presence of a complex magnetic ordering phenomenon below 0.3 K in this spin-orbit-driven frustrated magnet. The observed results demonstrate that the investigated kagome magnet is located in the close proximity of a quantum critical point. Further studies on the single crystals focusing on the effect of external perturbations such as chemical and hydrostatic pressure may provide vital clues concerning the exotic magnetism and spin dynamics in this frustrated magnet. The present family of spin-orbit-driven rare-earth distorted kagome series RE_3BWO_9 offers a viable ground for the experimental realization of exotic quantum states and establishing a realistic microscopic Hamiltonian in this class of quantum materials.

ACKNOWLEDGEMENTS

P. K. acknowledges funding by the Science and Engineering Research Board and Department of Science and Technology, India through research grants. A. Y. thanks M. Barik for the help in synthesizing a batch of polycrystalline sample. A. Z. acknowledges the financial support of the Slovenian Research and Innovation Agency through the Programme No. P1-0125 and Projects Nos. J1-50008 and N1-0148. R. K. and A. E. acknowledge the financial support by DFG under Germany's Excellence Strategy EXC2181/1-390900948 (the Heidelberg STRUCTURES Excellence Cluster) and through the DAAD GSSP program D. T. A. acknowledges funding from EPSRC-UK (Grant No. EP/W00562X/1). We acknowledge ISIS STFC neutron and PSI muon Facilities for beam time proposals. We acknowledge the support of the HLD at HZDR, a member of the European Magnetic Field Laboratory.

Appendix-A: CEF parameters

In this appendix, we discuss the CEF parameters obtained from simultaneously fitting the INS spectra at 5 K and single crystal susceptibility data. The crystal structure of Nb_3BWO_9 is hexagonal, however, the point symmetry of the Nd ion is triclinic C_1 . Due to this low point symmetry of Nd ion the CEF Hamiltonian has total of 27 independent CEF parameters. This makes it challenging to estimate all CEF parameters by fitting the INS data only. Thus, first, we use a grid searching program to find the best values of 27 CEF parameters, which can fit four CEF energies and their intensities. This search gave the best solution with minimum χ^2 . We use this set as starting set of CEF parameters and fitted together the INS and single crystal susceptibility data by only varying three CEF parameters, B_2^0, B_2^1, B_2^2 and keeping rest of CEF parameters fix from our search method. This method gave very good fit to the INS and single crystal susceptibility data and the fits are shown in Fig. 2. The values of the obtained CEF parameters are given in the table below.

Table-II

The values of the CEF parameters in meV. The I before the parameters (i.e. IB_2^1) indicates that they are imaginary terms (sometimes called “sine” terms).

$B_2^0 = -0.0309$	$B_6^2 = 0.00085$	$IB_{44} = -0.0170$
$B_2^1 = 0.2433$	$B_6^3 = 0.00079$	$IB_6^1 = 0.0010,$
$B_2^2 = -0.0693$	$B_6^4 = 0.0010$	$IB_6^2 = 0.0010$
$B_2^0 = -0.0027$	$B_6^5 = -0.0031$	$IB_6^3 = 0.0015$
$B_4^1 = 0.0058$	$B_6^6 = 0.0012$	$IB_6^4 = -0.0011$
$B_4^2 = -0.0137$	$IB_2^1 = -0.2934$	$IB_6^5 = 0.00204$
$B_4^3 = 0.0378$	$IB_2^2 = -0.1272$	$IB_6^6 = -0.0018$
$B_4^4 = -0.01102$	$IB_4^1 = -0.0208$	$IB_4^2 = -0.0086$
$B_6^0 = 0.00005$	$B_6^1 = 0.0010$	$IB_4^3 = 0.0618$

Table III

CEF energy levels (in meV) for the CEF model.

E_0	E_1	E_2	E_3	E_4
0	16.0197	33.138	42.699	58.703

- [1] Introduction to Frustrated Magnetism: Materials, Experiments, Theory, edited by C. Lacroix, P. Mendels, and F. Mila, Springer Series in Solid-State Sciences Vol. 164 (Springer, New York, 2011).
- [2] L. Balents. Spin liquids in frustrated magnets. *Nature* **464**, 199 (2010).
- [3] J. Khatua, B. Sana, A. Zorko, M. Gomilšek, K. Sethupathi, M. R. Rao, M. Baenitz, B. Schmidt, and P. Khuntia. Experimental signatures of quantum and topological states in frustrated magnetism. *Phys. Rep.* **1041**, 1 (2023).
- [4] T. Arh, B. Sana, M. Pregelj, P. Khuntia, Z. Jagličić, M. D. Le, P. K. Biswas, P. Manuel, L. Mangin-Thro, A. Ozarowski, and A. Zorko. The Ising triangular-lattice antiferromagnet neodymium heptatantalate as a quantum spin liquid candidate. *Nat. Mater.* **21**, 416 (2022).
- [5] W. Witczak-Krempa, G. Chen, Y. B. Kim, and L. Balents. Correlated quantum phenomena in the strong spin-orbit regime. *Annu. Rev. Condens. Matter Phys.* **5**, 57 (2014).
- [5] M. Vojta. Frustration and quantum criticality. *Rep. Prog. Phys.* **81**, 064501 (2018).
- [6] H. Takagi, T. Takayama, G. Jackeli, G. Khaliullin, and S. E. Nagler. Kitaev quantum spin liquid - concept and materialization. *Nat. Rev. Phys.* **1**, 264 (2019).
- [7] C. Broholm, R.J. Cava, S.A. Kivelson, D.G. Nocera, M.R. Norman, T. Senthil. Quantum spin liquids. *Science* **367**, eaay0668 (2020).
- [8] L. Savary, L. Balents. Quantum spin liquids: a review. *Rep. Progr. Phys.* **80**, 016502 (2017).
- [9] Y. Zhou, K. Kanoda, T.-K. Ng. Quantum spin liquid states. *Rev. Modern Phys.* **89**, 025003 (2017).
- [10] X.-G. Wen. Choreographed entanglement dances: Topological states of quantum matter. *Science* **363**, eaal3099 (2019).
- [11] S. Yan, D. A. Huse, and S. R. White. Spin-Liquid Ground State of the $S = 1/2$ Kagome Heisenberg Antiferromagnet. *Science* **332**, 1173 (2011).
- [12] P. Khuntia, M. Velazquez, Q. Barthélemy, F. Bert, E. Kermarrec, A. Legros, B. Bernu, L. Messio, A. Zorko, and P. Mendels. Gapless ground state in the archetypal quantum kagome antiferromagnet $\text{ZnCu}_3(\text{OH})_6\text{Cl}_2$. *Nature Physics* **16**, 469 (2020).
- [13] K. Matan, T. Ono, Y. Fukumoto, T. J. Sato, J. Yamaura, M. Yano, K. Morita, and H. Tanaka. Pinwheel valence-bond solid and triplet excitations in the two-dimensional deformed kagome lattice. *Nat. Phys.* **6**, 865 (2010).
- [14] S. Ishiwata, D. Wang, T. Saito, and M. Takano. High-Pressure Synthesis and Structure of $\text{SrCo}_6\text{O}_{11}$: Pillared Kagomé Lattice System with a $1/3$ Magnetization Plateau. *Chem. Mater.* **17**, 2789 (2005).

- [15] Z. Guguchia, H. Zhou, C. N. Wang, J.-X. Yin, C. Mielke III, S. S. Tsirkin, I. Belopolski, S.-S. Zhang, T. A. Cochran, T. Neupert, R. Khasanov, A. Amato, S. Jia, M. Z. Hasan, and H. Luetkens. Multiple quantum phase transitions of different nature in the topological kagome magnet $\text{Co}_3\text{Sn}_{2-x}\text{In}_x\text{S}_2$. *npj Quantum Materials* **6**:50 (2021).
- [16] S. S. Gong, W. Zhu, L. Balents, and D. N. Sheng. Global phase diagram of competing ordered and quantum spin-liquid phases on the kagome lattice. *Phys. Rev. B* **91**, 075112 (2015).
- [17] L. Ye et al. Massive Dirac fermions in a ferromagnetic kagome metal. *Nature* **555**, 638 (2018).
- [18] D. Guterding, H. O. Jeschke, R. Valentí. Prospect of quantum anomalous Hall and quantum spin Hall effect in doped kagome lattice Mott insulators. *Sci. Rep.* **6**, 25988 (2016).
- [19] A. Petrescu, A. A. Houck, and K. L. Hur. Anomalous Hall effects of light and chiral edge modes on the Kagomé lattice. *Phys. Rev. A* **86**, 05380 (2012).
- [20] X. Li et al. Field-linear anomalous Hall effect and Berry curvature induced by spin chirality in the kagome antiferromagnet Mn_3Sn . *Nat Commun* **14**, 1642 (2023).
- [21] H. Chen et al. Roton pair density wave in a strong-coupling kagome superconductor. *Nature* **599**, 222 (2021).
- [22] Z. Guguchia et al. Unconventional charge order and superconductivity in kagome-lattice systems as seen by muon-spin rotation. *npj Quantum Mater.* **8**, 41 (2023).
- [23] G. Semeghini et al. Probing topological spin liquids on a programmable quantum simulator. *Science* **374**, 1242 (2021).
- [24] A. Hutter, J.R. Wootton, and D. Loss. Parafermions in a Kagome Lattice of Qubits for Topological Quantum Computation. *Phys. Rev. X* **5**, 041040 (2015).
- [25] G. Misguich and P. Sindzingre. Magnetic susceptibility and specific heat of the spin-1/2 Heisenberg model on the kagome lattice and experimental data on $\text{ZnCu}_3(\text{OH})_6\text{Cl}_2$. *Eur. Phys. J. B* **59**, 305 (2007).
- [26] B. Bernu, L. Pierre, K. Essafi, and L. Messio. Effect of perturbations on the kagome $S=1/2$ antiferromagnet at all temperatures. *Phys. Rev. B* **101**, 140403 (2020).
- [27] R. R. P. Singh. Valence Bond Glass Phase in Dilute Kagome Antiferromagnets. *Phys. Rev. Lett.* **104**, 177203 (2010).
- [28] O. Cepas, C. M. Fong, P. W. Leung, and C. Lhuillier. Quantum phase transition induced by Dzyaloshinskii-Moriya interactions in the kagome antiferromagnet. *Phys. Rev. B* **78**, 140405 (R) (2008).
- [29] A. Zorko, M. Herak, M. Gomilšek, J. van Tol, M. Velázquez, P. Khuntia, F. Bert, and P. Mendels. Symmetry Reduction in the Quantum Kagome Antiferromagnet Herbertsmithite. *Phys. Rev. Lett.* **118**, 017202 (2017).

- [30] P. Mendels et al. Quantum Magnetism in the Paratacamite Family: Towards an Ideal Kagomé Lattice. *Phys. Rev. Lett.* **98**, 077204 (2007).
- [31] T. Arh, M. Gomilsek, P. Prelovsek, M. Pregelj, M. Klanjsek, A. Ozarowski, S. J. Clark, T. Lancaster, W. Sun, J.-X. Mi, and A. Zorko. Origin of Magnetic Ordering in a Structurally Perfect Quantum Kagome Antiferromagnet. *Phys. Rev. Lett.* **125**, 027203 (2020).
- [32] T. F. Seman, C.-C. Chen, R. R. P. Singh, and M. van Veenendaal. The many faces of quantum kagome materials: Interplay of further-neighbour exchange and Dzyaloshinskii-Moriya interaction. arXiv:1508.01523.
- [33] J. Colbois, B. Vanhecke, L. Vanderstraeten, A. Smerald, F. Verstraete, and F. Mila, Partial lifting of degeneracy in the J_1 - J_2 - J_3 Ising antiferromagnet on the kagome lattice. *Phys. Rev. B* **106**, 174403 (2022).
- [34] W.-J. Hu, W. Zhu, Y. Zhang, S. Gong, F. Becca, and D. N. Sheng. Variational Monte Carlo study of a chiral spin liquid in the extended Heisenberg model on the kagome lattice. *Phys. Rev. B* **91**, 041124(R) (2015).
- [35] Y. Tokiwa, C. Stingl, M.-S. Kim, T. Takabatake, P. Gegenwart. Characteristic signatures of quantum criticality driven by geometrical frustration. *Sci. Adv.* **1**:e1500001(2015).
- [36] B. Gao, T. Chen, D. Tam, C.-L. Huang, K. Sasmal, D. Adroja, F. Ye, H. Cao, G. Sala, M. Stone, C. Baines, J. Barker, H. Hu, J.-H. Chung, X. Xu, S.-W. Cheong, M. Nallaiyan, S. Spagna, M. Maple, and P. Dai. Experimental signatures of a three-dimensional quantum spin liquid in effective spin-1/2 $\text{Ce}_2\text{Zr}_2\text{O}_7$ pyrochlore. *Nat. Phys.* **15**, 1052 (2019).
- [37] Z. F. Ding et al. Possible gapless spin liquid in the rare-earth kagome lattice magnet $\text{Tm}_3\text{Sb}_3\text{Zn}_2\text{O}_{14}$. *Phys. Rev. B* **98**, 174404 (2018).
- [38] Z. Ma et al. Disorder-induced spin-liquid-like behavior in kagome-lattice compounds. *Phys. Rev. B* **102**, 224415 (2020).
- [39] A. Zorko et al. Easy-Axis Kagome Antiferromagnet: Local-Probe Study of $\text{Nd}_3\text{Ga}_5\text{SiO}_{14}$. *Phys. Rev. Lett.* **100**, 147201 (2008).
- [40] Z. Hu et al. Evidence of the Berezinskii-Kosterlitz-Thouless phase in a frustrated magnet. *Nat. Commun.* **11**, 5631 (2020).
- [41] W.-Y. Su, F. Hu, C. Cheng, and N. Ma. Berezinskii-Kosterlitz-Thouless phase transitions in a kagome spin ice by a quantifying Monte Carlo process: Distribution of Hamming distances. *Phys. Rev. B* **108**, 134422 (2023).
- [42] Aleksii Julku, Georg M. Bruun, and Päivi Törmä. Quantum Geometry and Flat Band Bose-Einstein Condensation. *Phys. Rev. Lett.* **127**, 170404 (2021).
- [43] K Górnicka et al., Superconductivity in a breathing kagome metals RO_2 ($\text{R} = \text{Sc}, \text{Y}, \text{Lu}$). *Sci Rep.* **13**, 16704 (2023).

- [44] M. Ashtar, J. Guo, Z. Wan, Y. Wang, G. Gong, Y. Liu, Y. Su, and Z. Tian, A New Family of Disorder-Free Rare-Earth-Based Kagome Lattice Magnets: Structure and Magnetic Characterizations of RE₃BWO₉ (RE = Pr, Nd, Gd--Ho) Boratotungstates. *Inorg. Chem.* **59**, 5368 (2020).
- [45]. L.-L. Li, X.-Y. Yue, W.-J. Zhang, H. Bao, D.-D. Wu, H. Liang, Y.-Y. Wang, Y. Sun, Q.-J. Li, and X.-F. Sun, Magnetism and giant magnetocaloric effect in rare-earth-based compounds R₃BWO₉ (R = Gd, Dy, Ho). *Chin. Phys. B* **30**, 077501 (2021).
- [46]. K. -Y. Zeng, F. Y. Song, Z. M. Tian, Q. Chen, S. Wang, B. Liu, S. Li, L. S. Ling, W. Tong, L. Ma, and L. Pi. Local evidence for collective spin excitations in the distorted kagome antiferromagnet Pr₃BWO₉. *Phys. Rev. B* **104**, 155150 (2021).
- [47] K. -Y. Zeng et al. Incommensurate Magnetic Order in Sm₃BWO₉ with Distorted Kagome Lattice. *Chin. Phys. Lett.* **39**, 107501 (2022).
- [48]. D. Flavian, J. Nagl, S. Hayashida, M. Yan, Q. Zaharko, T. Fennell, D. Khalyavin, Z. Yan, S. Gvasaliya, and A. Zheludev. Magnetic phase diagram of the breathing-kagome antiferromagnet Nd₃BWO₉. *Phys. Rev. B* **107**, 174406 (2023).
- [49] F. Song et al. Magnetic field tuned anisotropic quantum phase transition in the distorted kagome antiferromagnet Nd₃BWO₉. *Phys. Rev. B* **108**, 214410 (2023).
- [50] J. Nagl et al. Excitation spectrum and spin Hamiltonian of the frustrated quantum Ising magnet Pr₃BWO₉. *Phys. Rev. Research* **6**, 023267 (2024).
- [51] V. A. Krut'ko, A. A. Belik & G. V. Lysanova. Structures of Nonlinear Hexagonal Boratotungstates Ln₃BWO₉ (Ln = La, Pr, Nd, Sm, Gd, Tb, Dy). *Russ. J. Inorg. Chem.* **51**, 884 (2006).
- [52] Y. Skourski, M. D. Kuz'min, K. P. Skokov, A. V. Andreev, and J. Wosnitza. High-field magnetization of Ho₂Fe₁₇. *Phys. Rev. B* **83**, 214420 (2011).
- [53] A. A. Suter and B. M. Wojek, Musrfit: A Free Platform-Independent Framework for μ SR Data Analysis. *Phys. Procedia* **30**, 69 (2012).
- [54] T. Besara et al. Single crystal synthesis and magnetism of the BaLn₂O₄ family (Ln = lanthanide). *Prog. Solid State Chem.* **42**, 23 (2014).
- [55] P. Khuntia and D. T. Adroja, Novel ground state in the rare-earth based kagome antiferromagnets, STFC ISIS Neutron and Muon Source. <https://doi.org/10.5286/ISIS.E.RB2220746> (2022).
- [56] A. Elghandour, PhD Thesis (2023), University of Heidelberg, Germany.
- [57] R. Orbach. Spin-Lattice Relaxation in Rare-Earth Salts. *Proc. R. Soc. London A* **264**, 458 (1961).
- [58] A. Yaouanc and P. Dalmas de Réotier. *Muon Spin Rotation, Relaxation, and Resonance: Applications to Condensed Matter* (Oxford University Press, Oxford, 2011).

- [59] D.T. Adroja, A. Bandyopadhyay, H. Leutkens, T.J. Hicken, J.A. Krieger, G. B. Stenning, Z. Tian, S. Li et al (*Private Communications*)
- [60] M. Hiraishi et al., Nonmagnetic Ground State in RuO₂ Revealed by Muon Spin Rotation. *Phys. Rev. Lett.* **132**, 166702 (2024).
- [61] P. Kessler et al., Absence of magnetic order in RuO₂: insights from μ SR spectroscopy and neutron diffraction. arXiv:2405.10820.
- [62] A. Amato et al. Magnetic and Superconducting Properties of the Heavy-Fermion Superconductor UPd₂Al₃. *Eur. Phys. Lett.* **19**, 127 (1992).
- [63] L. Balents, M. P. A. Fisher, and S. M. Girvin, Fractionalization in an easy-axis Kagome antiferromagnet, *Phys. Rev. B* **65**, 224412 (2002).
- [64] B. Canals et al. Fragmentation of magnetism in artificial kagome dipolar spin ice. *Nat. Comm.* **7**, 11446 (2016).
- [65] A. Zorko, F. Bert, P. Mendels, A. Potočnik, A. Amato, C. Baines, K. Marty, P. Bordet, P. Lejay, E. Lhotel, V. Simonet, R. Ballou Quantum Tunneling in Half-Integer-Spin Kagome-Lattice Langasites. arXiv:1210.8187
- [66] M. Ulaga, J. Kokalj, A. Wietek, A. Zorko, and P. Prelovšek. Finite-temperature properties of the easy-axis Heisenberg model on frustrated lattices. *Phys. Rev. B* **109**, 035110 (2024).
- [67] T. Moriya, *Spin Fluctuations in Itinerant Electron Magnetism* (Springer-Verlag: Berlin, Heidelberg, 1985).
- [68] N. Bloembergen, E. M. Purcell, and R. V. Pound. Nuclear Magnetic Relaxation. *Nature* **160**, 475 (1947).
- [69] J. Dorier, K. P. Schmidt, and F. Mila. Theory of Magnetization Plateaux in the Shastry-Sutherland Model. *Phys. Rev. Lett.* **101**, 250402 (2008).
- [70] A. Sen, K. Damle, and A. Vishwanath. Magnetization Plateaus and Sublattice Ordering in Easy-Axis Kagome Lattice Antiferromagnets. *Phys. Rev. Lett.* **100**, 097202 (2008)
- [71] M. J. R Hoch, H. D. Zhou, E. Mun, and N. Harrison. Pulsed field magnetization in rare-earth kagome systems. *J. Phys.: Condens. Matter* **28**, 046001 (2016).
- [72] A. Honecker, J. Schulenburg and J. Richter. Magnetization plateaus in frustrated antiferromagnetic quantum spin models. *J. Phys.: Condens. Matter* **16**, S749 (2004).
- [73] A. Sen, F. Wang, K. Damle and R. Moessner. Triangular and Kagome Antiferromagnets with a Strong Easy-Axis Anisotropy. *Phys. Rev. Lett.* **102**, 227001 (2009).